This article has been accepted for inclusion in a future issue of this journal. Content is final as presented, with the exception of pagination.

Passive Intermodulation in Metal-to-Metal Contacts Caused by Tunneling Current

Amir Dayan, Yi Huang, *Fellow, IEEE*, Mattias Gustafsson, Torbjörn Olsson, *Member, IEEE*, and Alexander G. Schuchinsky, *Fellow, IEEE*

***Abstract*— Passive intermodulation (PIM) by metal contacts limits the bandwidth and capacity of radio links used in mobile and satellite communications. In this work, we investigate the effect of nonlinearities in metal-insulator-metal (MIM) contacts and their effects on PIM generation. An analytical expression is obtained for the tunneling current density which has an error of ∼1.6% in the case of a very thin insulator and low voltages in MIM junctions. The presented analytical model of the contact surfaces with the fractal geometry is used to simulate PIM products of third-order (PIM3) and fifth-order (PIM5) versus the contact resistance and applied pressure. The simulation results are validated experimentally by an open-ended rectangular coaxial structure with a slotted enclosure. The measurement results demonstrate that the presented model predicts the PIM with a mean error of about 4.8 dB when the contact pressure varies from 0.5 to 1.7 MPa.**

***Index Terms*— Contact nonlinearity, metal-insulator-metal (MIM) junction, metal-to-metal contact, passive intermodulation (PIM), signal distortion, tunneling current.**

I. Introduction

PASSIVE intermodulation (PIM) in communication systems and their components has been the subject of intensive studies for more than 50 years [1], [2], [3], [4], [5], [6], [7], [8], [9], [10], [11]. PIM in conductor joints and connectors which is primarily caused by their nonlinear voltage-current relations [12], [13], [14], [15] has recently attracted particular attention. Several different mechanisms of nonlinearity may coexist and include charge tunneling [13], [16], the electro-thermal effect [17], thermionic emission [12], [13], Fowler–Nordheim electron transmission [18], [19], and mechanical deformations [20]. However, the electro-thermal effect is notable only when the high-power carrier frequencies are very close to each other and the mechanical deformations develop very slowly. Also, the Fowler–Nordheim current appears only at an extremely high electric field exceeding 1 GV/m, whilst the thermionic emission occurs at temperatures above 1000 K. Therefore, the tunneling current in metal-insulator-metal (MIM) junctions is the dominant nonlinear effect at RF frequencies. In the case of a very small contact area, commensurate with the electron-free path in metal, the charge flow is constricted and manifests itself in higher resistance. This effect can be described by Maxwell Sharvin resistance [21] which is smaller than the tunneling resistance of the oxide layer in MIM junctions.

Manuscript received 28 August 2023; revised 10 November 2023 and 12 January 2024; accepted 16 January 2024. This work was supported by Huawei Technologies Sweden AB. *(Corresponding author: Yi Huang.)*

Amir Dayan, Yi Huang, and Alexander G. Schuchinsky are with the Department of Electrical Engineering and Electronics, University of Liverpool, Liverpool, L69 3BX Liverpool, U.K. (e-mail: amir.dayan@liverpool.ac.uk; huangyi@liverpool.ac.uk; aschuch@liverpool.ac.uk).

Mattias Gustafsson and Torbjörn Olsson are with Huawei Technologies Sweden AB, 412 50 Gothenburg, Sweden (e-mail: mattias.gustafsson@huawei.com; torbjorn.olsson@huawei.com).

Color versions of one or more figures in this article are available at https://doi.org/10.1109/TMTT.2024.3363885.

Digital Object Identifier 10.1109/TMTT.2024.3363885

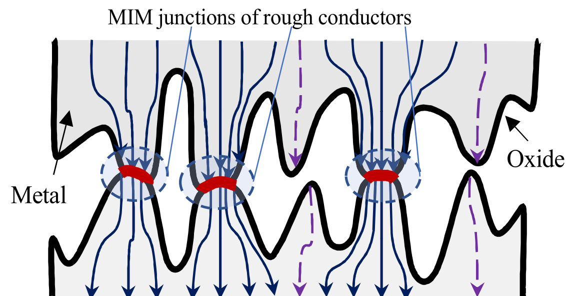

Fig. 1. MIM contact junction of conductors with rough surfaces. Thin insulator films at the contact spots of asperity tips are shown in red.

Charge tunneling in MIM junctions plays an important role in the contacts of good conductors because its timescale is commensurate with the periodicity of the high-power RF signals. This effect determines how the charges flow through extremely thin films of oxide in contact joints. The electron transmission in MIM junctions is usually described by the Wentzel–Kramers–Brillouin (WKB) approximation [22]. Based on this model and the Fermi–Dirac distribution of electrons inside the metal, Holm [12] and Simmons [13] have obtained the simplified voltage-current relations for ideal MIM junctions. Simmons model proved to be fairly accurate for oxide layers thicker than 2 nm. But at thin oxide layers, commensurate with a few lattice constants, Simmons model falters and must be refined.

As shown in Fig. 1, the actual contact area of rough surfaces is always smaller than its nominal area [23]. This is the result of surface roughness, which can be described by Gaussian or Weierstrass–Mandelbrot (WM) distributions [20], [23], [24], [25], [26], [27], [28], [29], [30], [31], [32], [33], [34], [35], [36], [37]. These patterns of contact asperities have been used for evaluating the contact resistance of micro-electromechanical systems (MEMS) [20], [29], [30], [31], [32], [33], [34], [35], [36], [37]. Nonlinearities of the contact joints of rough conductors have recently attracted significant interest in the waveguide flanges, conductor joints, and connectors [6], [38], [39], [40]. The effect of the surface

0018-9480 © 2024 IEEE. Personal use is permitted, but republication/redistribution requires IEEE permission.
See https://www.ieee.org/publications/rights/index.html for more information.

Authorized licensed use limited to: University of Liverpool. Downloaded on February 18,2024 at 11:08:21 UTC from IEEE Xplore. Restrictions apply.

This article has been accepted for inclusion in a future issue of this journal. Content is final as presented, with the exception of pagination.

roughness of the waveguide flanges was investigated in [6]. It was demonstrated that the contact pressure and the flange deformations might considerably affect the contact nonlinearity. The nonlinear behavior of the coaxial connectors with rough surfaces of the contact joints was studied in [40]. The model [40], based on the Simmons approximation and Ansys simulation of contact mechanics, has shown a reasonable correlation with the measured PIM products.

In this work, the Simmons model is extended and validated experimentally. The developed test setup enables PIM products of third-order (PIM3) and fifth-order (PIM5) measurements. The model accuracy is confirmed by the PIM3 and PIM5 measurements of the dedicated test fixture.

The article is organized as follows. A proposed modified model of the MIM junction with thin insulating layer and its analysis are presented in Section II. The effects of mechanical deformations are discussed in Section III. In Section IV, an equivalent electric circuit of the contact surfaces is presented. Section V describes the measurement setup for the 700 MHz band and presents a comparison between the simulations and measurements. The Conclusions summarize the main results.

II. Model of MIM Junction

In MIM contacts with a thin insulator layer of nanometer thickness, electrons can tunnel through the potential barrier and sustain an electric current. The probability that electrons with energy U pass through a potential barrier can be described by WKB approximation as [13].

$$\Im(U) = \exp\left(-\frac{4\pi}{h}\int_{s_1}^{s_2}\sqrt{2m(\eta+\varphi(x)-U)}dx\right) \quad (1)$$

where h is Planck constant, $s_{1,2}$ are the bounds of the potential barrier at the Fermi level η of the metal, m is the mass of an electron, x is the coordinate inside an insulating layer, and $\varphi(x)$ is the potential barrier taking into account the image potential [13].

$$\begin{aligned}\varphi(x) &= \varphi_0 - \frac{x}{s}eV_g - \frac{e^2}{4\pi\varepsilon}\left(\frac{1}{2x}+\sum_{n=1}^{\infty}\frac{x^2}{ns\left[(ns)^2-x^2\right]}\right)\\ &= \varphi_0 - \frac{x}{s}eV_g + \frac{e^2}{4\pi\varepsilon s}\left[C_E+\psi\left(\frac{x}{s}\right)+\frac{\pi}{2}\cot\left(\pi\frac{x}{s}\right)\right]\end{aligned} \quad (2)$$

φ_0 is the potential barrier height above the Fermi level of metal, V_g is the external voltage between the electrodes in the MIM junction, e is the electron charge, s is the physical thickness of the oxide layer with permittivity ε, $C_E = 0.577215665$ is Euler's constant, and $\psi(u)$ is the psi-function. The last term in (2) represents an image potential that reduces the height and width of the potential barrier $\varphi(x)$. Its effect is particularly notable for small thicknesses s of the insulating layer, as will be discussed later.

The integral (1) cannot be evaluated analytically and $\Im(U)$ is approximated in [13] as

$$\tilde{\Im}(U, V_g) \approx \exp\left(-A\sqrt{\eta+\bar{\varphi}(V_g)-U}\right) \quad (3)$$

where $A = 4\pi\Delta s(2m)^{1/2}/h$, $\Delta s = s_2 - s_1$, $\bar{\varphi}(V_g)$ is the average height of the potential barrier $\phi(x)$ of the insulating layer. When voltage V_g, applied to the MIM junction, is smaller than $\max\{\varphi(x)\}$, $\phi(x)$ is approximated as $\bar{\varphi}(V_g) = \bar{\varphi}_0 - eV_g/2$, where $\bar{\varphi}_0$ is the average height of the potential barrier at zero external bias. Then the current density in a contact junction is

$$\tilde{j}(V_g) = e\int_0^{E_m}\tilde{\Im}(U, V_g)[N_1(U)-N_2(U)]dU \quad (4)$$

where E_m is the maximum energy of electrons which depends on their energies in conductors and $E_m = \eta$ at zero temperature. $N_1(U)dU$ and $N_2(U)dU$ are the numbers of electrons in each conductor with an energy level between U and $U + dU$, where $N_1(U)$ and $N_2(U)$ are [15].

$$\begin{aligned}N_1(U) &= \frac{4m\pi kT}{h^3}\ln\left[1+\exp\left(-\frac{U-\eta}{kT}\right)\right]\\ N_2(U) &= \frac{4m\pi kT}{h^3}\ln\left[1+\exp\left(-\frac{U+eV_g-\eta}{kT}\right)\right]\end{aligned} \quad (5)$$

where k is the Boltzmann's constant. When temperature T approaches zero, $N_1(U)$ and $N_2(U)$ become step functions and $\tilde{j}(V_g)$ is obtained in closed form

$$\begin{aligned}\tilde{j}(V_g) &= \frac{4\pi me}{h^3}\left[\begin{array}{l} eV_g\int_0^{\eta-eV_g}\exp\left(-A\sqrt{\eta+\bar{\varphi}(V_g)-U}\right)dU\\ +\int_{\eta-eV_g}^{\eta}(\eta-U)\exp\left(-A\sqrt{\eta+\bar{\varphi}(V_g)-U}\right)dU\end{array}\right]\\ &= \kappa\left[\begin{array}{l}\xi\left(\bar{\varphi}(V_g)\right)\exp\left(-A\sqrt{\bar{\varphi}(V_g)}\right)\\ -\xi\left(\bar{\varphi}(V_g)+eV_g\right)\exp\left(-A\sqrt{\bar{\varphi}(V_g)+eV_g}\right)\\ -\frac{A^2eV_g}{2}\left(A\sqrt{\eta+\bar{\varphi}(V_g)}+1\right)\exp\left(-A\sqrt{\eta+\bar{\varphi}(V_g)}\right)\end{array}\right]\end{aligned} \quad (6)$$

where $\xi(\theta) = (A(\theta)^{1/2})^2 + 3A(\theta)^{1/2} + 3$, $\kappa = (16\pi me/A^4h^3)$. The last term in (6) is small at $\eta > \bar{\varphi}(V_g)$ and can be neglected [13]. Then, the tunneling current density $\tilde{j}(V_g)$ in the MIM junction becomes

$$\tilde{j}(V_g) \simeq j_0\left[\upsilon\left(\bar{\varphi}(V_g)\right) - \upsilon\left(\bar{\varphi}(V_g)+eV_g\right)\right] \quad (7)$$

where $j_0 = e/2\pi h\Delta s^2$, and

$$\upsilon(u) = u\exp\left(-A\sqrt{u}\right)\left[1+3\frac{A\sqrt{u}+1}{\left(A\sqrt{u}\right)^2}\right]. \quad (8)$$

At $\Delta s \geq 2$ nm, the last term in the square bracket of (8) rapidly decays and becomes small. Then (7) is reduced to the Simmons equation [13]. However, at $\Delta sc\sim$ 1 nm, both terms in the square bracket of (8) are commensurate and must be retained. The tunneling current dependence on the contact voltage V_g is shown in Fig. 2, where approximation (7) and the Simmons model are compared with the numerical calculation by WKB method. The simulation results show that approximation (7) is close to WKB method at small s and low voltages. But the difference increases when voltage bias V_g becomes larger and the effective thickness s of insulator become smaller as demonstrated by Fig. 2 and in Table I. Simmons model and approximation (7) follow the same trends

Authorized licensed use limited to: University of Liverpool. Downloaded on February 18,2024 at 11:08:21 UTC from IEEE Xplore. Restrictions apply.

This article has been accepted for inclusion in a future issue of this journal. Content is final as presented, with the exception of pagination.

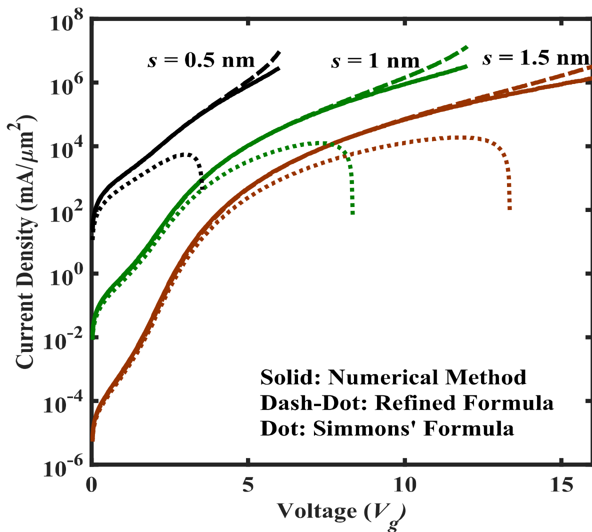

Fig. 2. Tunneling current density in MIM junctions for $\varphi_0 = 2$ eV and $\varepsilon_r = 9.3$ at different thicknesses s of insulating layers. At small voltages, refined (7) is in agreement with the numerical analysis based on WKB approximation (1).

TABLE I
CURRENT AS A FUNCTION OF VOLTAGE

	$V_g = 1$ V			$V_g = 5$ V		
s, nm	$j_{WKB}(V_g)$	$\tilde{j}(V_g)$	$j_S(V_g)$	$j_{WKB}(V_g)$	$\tilde{j}(V_g)$	$j_S(V_g)$
0.5	1.20×10^3	1.18×10^3	522.95	7.96×10^5	1.13×10^6	-
1.0	0.85	0.78	0.58	1.05×10^4	1.03×10^4	3.31×10^3
1.5	9.18×10^4	7.96×10^4	6.60×10^4	480.85	462.93	241.70

Current densities in mA/μm² calculated at voltage biases 1V and 5V: $j_{WKB}(V_g)$ - WKB approximation, $\tilde{j}(V_g)$ - eqn. (7), and $j_S(V_g)$ - Simmons model.

in Fig. 2 but their current densities differ. The numerical estimates in Table I at $V_g = 1$ V and $V_g = 5$ V show that the current densities calculated by the Simmons model have a bigger error as compared to the refined model (7). Table I shows that the error of (7) is 1.6%, 8.2%, and 13.3% at the 1 V bias and oxide thicknesses of 0.5, 1, and 1.5 nm, whereas the errors of the Simmons equation are 56.4%, 31.7%, and 28.1%, respectively.

It is necessary to note that both the Simmons model and (7) are valid only in the limited range of V_g. This is evident in Fig. 2 where the current density, calculated by the Simmons model suddenly drops and deviates from the WKB model.

At low voltages V_g, $\bar{\varphi}(V_g) \simeq \bar{\varphi}_0 - eV_g/2$, $\tilde{j}(V_g)$ can be approximated by a few terms of the series expansion of (7)

$$\tilde{j}(V_g) = g_1 V_g + g_3 V_g^3 + g_5 V_g^5 + O\left(V_g^7\right) \tag{9}$$

where

$$g_1 = m\pi e^2 \frac{8\left(1 + A\sqrt{\bar{\varphi}_0}\right)}{A^2 h^3} \exp\left(-A\sqrt{\bar{\varphi}_0}\right) \tag{10}$$

$$g_3 = m\pi e^4 \frac{A}{12\sqrt{\bar{\varphi}_0} h^3} \exp\left(-A\sqrt{\bar{\varphi}_0}\right) \tag{11}$$

$$g_5 = m\pi e^6 \frac{A\left(A^2\bar{\varphi}_0 + 3\left(A\sqrt{\bar{\varphi}_0} + 1\right)\right)}{3840\bar{\varphi}_0^{5/2} h^3} \exp\left(-A\sqrt{\bar{\varphi}_0}\right). \tag{12}$$

Coefficient g_1 describes a linear conductance per unit area of the MIM junction whilst g_3 and g_5 describe the contact nonlinearity. Then PIM products generated by MIM junctions at the asperity contacts are evaluated with approximation (9).

III. CONTACT DEFORMATIONS OF ASPERITIES

A. Profile of Rough Surfaces

The surface roughness profile is described by WM distribution [26], [27], [28]. WM function is self-affine but not differentiable that is compatible with the contacts of rough surfaces. The surface profile is described as [28].

$$\begin{aligned} z(x, y) &= L\left(\frac{G}{L}\right)^{(D-2)} \left(\frac{\ln\gamma}{M}\right)^{1/2} \sum_{m=1}^{M} \sum_{n=0}^{n_{\max}} \gamma^{(D-3)n} \\ &\times \left\{ \cos(\phi_{m,n}) - \cos\left[\frac{2\pi\gamma^n\sqrt{x^2+y^2}}{L} \cos \right.\right. \\ &\left.\left. \times \left(\tan^{-1}\left(\frac{y}{x}\right) - \frac{m\pi}{M}\right) + \phi_{m,n}\right]\right\} \end{aligned} \tag{13}$$

where $z(x, y)$ is a profile of the asperity heights, L is the sample length, G is fractal roughness that is a scaling parameter independent of frequency, D is the fractal dimension ($2 < D < 3$), $\varphi_{m,n}$ is a random phase varying between 0 and 2π, M is the number of superposed ridges used to construct a surface, and $n_{\max} = \text{int}[\log(L/L_s)/\log(\gamma)]$ is the index of the maximum asperity frequency corresponding to the sample length, L_s is a cut-off length, and γ is a scaling parameter (typically $\gamma \approx 1.5$), which depends on surface flatness and asperity distribution density.

B. Contact Area of Rough Surfaces

Surface profiles of the contact surfaces are described by WM distribution. They allow us to model the contacts under pressure and evaluate an actual contact area and contact resistance. This approach has been developed in [20], [29], [30], and [31], and it is briefly outlined here. Following [20], [29], Maxwell's conductance σ_H is represented as

$$\begin{aligned} \sigma_H &= \frac{A_a^{1/2}}{\rho_1 + \rho_2} \frac{2\sqrt{2}}{\sqrt{\pi}} \left(\frac{D-1}{D-2}\right) \left(a_L'^*\right)^{1/2} \\ &\times \left[\sqrt{2}\left(\frac{a_L'^*}{a_s'^*}\right)^{(D-2)/2} - \left(\sqrt{2}-1\right)\left(\frac{a_L'^*}{a_c'^*}\right)^{(D-2)/2} - 1\right] \end{aligned} \tag{14}$$

where A_a is a nominal contact area, $\rho_{1,2}$ are resistivities of the contact conductors, D is the fractal dimension of the surfaces, $a_L'^* = a_L'/A_a$, $a_s'^* = a_s'/A_a$, and $a_c'^* = a_c'/A_a$ are the normalized largest, smallest, and critical truncated areas, respectively. The critical truncated area a_c' is defined as the boundary between the elastic and plastic deformations

$$a_c' = \frac{\pi G^2}{4}\left[\frac{32}{b}\left(\frac{E}{KY}\right)^2 \ln\gamma\right]^{1/(D-2)} \tag{15}$$

where $E = [(1 - \upsilon_1^2)/E_1 + (1 - \upsilon_2^2)/E_2]^{-1}$ is the reduced elastic modulus, υ_1, υ_2 and E_1, E_2 are the Poisson's ratios and

Authorized licensed use limited to: University of Liverpool. Downloaded on February 18,2024 at 11:08:21 UTC from IEEE Xplore. Restrictions apply.

This article has been accepted for inclusion in a future issue of this journal. Content is final as presented, with the exception of pagination.

elastic moduli of the two surfaces, respectively; $b = (\pi k/2)^2$ with $k = 0.454 + 0.41 v_1$, v_1 is the Poisson ratio of the softer material; $K = 2.8$ is the ratio of material hardness to yield strength Y; γ and D are the adjustable parameters of the WM function; $a'_s = \pi r_s^2 \simeq \pi \cdot 10^{-6}\ \mu m^2$ at the radius of the smallest microcontact $r_s \sim 1$ nm that is commensurate with the lattice constants of good conductors [20].

The largest normalized size of the truncated contact area a'^*_L can be obtained numerically from (16) for the known force F applied to the contact and the small initial value of a'^*_L, varying between 0 and 1

$$F = A_a K Y \left(\frac{D-1}{3-D}\right) a'^*_L \left[\left(\frac{a'^*_c}{a'^*_L}\right)^{(3-D)/2} - \left(\frac{a'^*_s}{a'^*_L}\right)^{(3-D)/2}\right] + A_a E \frac{2^{9/2-D}}{3}\frac{D-1}{5/2-D}\sqrt{\ln\gamma}\left(\frac{G}{\sqrt{A_a}}\right)^{D-2}\left(\frac{a'^*_L}{\pi}\right)^{(4-D)/2} \times \left[1-\left(\frac{a'^*_c}{a'^*_L}\right)^{5/2-D}\right] \quad (16)$$

where K is the ratio of hardness to yield strength, Y is the yield strength (typically $K = 2.8$ and $Y \approx 300$ MPa), E is Young's modulus of the material, and γ is the adjustable parameter in the WM function. Once a'^*_L is obtained numerically from (16), the real contact area A_r is calculated for a given F as

$$A_r = \frac{A_a(D-1)}{2(3-D)} a'^*_L \left[\left(\frac{a'^*_c}{a'^*_L}\right)^{(3-D)/2} - 2\left(\frac{a'^*_s}{a'^*_L}\right)^{(3-D)/2} + 1\right]. \quad (17)$$

When the contact surfaces are oxidized, the contact resistance of a microcontact is determined by the charge tunneling described in Section II. Then the linear tunneling conductance is approximated as $\sigma_t = g_1 A_r$ where g_1 is defined in (10) and A_r in (17). Thus, σ_t can be readily taken into account at $\sigma_t \ll \sigma_H$.

IV. Equivalent Circuit Model of Contact Junction

Fig. 3(a) illustrates the equivalent circuit of the PIM measurement setup, which contains a RF source (described by P_s and Z_s), a transmission line with characteristic impedance Z_c, contact resistance R_t (tunneling resistance), capacitance C_L, and a low PIM load with impedance Z_L. Since the contact nonlinearity is weak, the source current in a matched circuit is evaluated at carrier frequency ω_k ($k = 1$, 2 denotes the first and second carriers, respectively) as

$$I_L(\omega_k) = \sqrt{\frac{2P_s(\omega_k)}{Z_L}} \quad (18)$$

where $P_s(\omega_k)$ represents the carrier power at frequency ω_k. Subsequently, the voltage drop of each carrier in the contact junction is calculated as

$$V_k = V(\omega_k) = \frac{R_1}{1 + j\omega_k C_L R_1} I_L(\omega_k) e^{-j\beta_k l} \quad (19)$$

where $\beta_k l$ is the phase change due to carrier transmission from the source (PIM analyzer) to the contact point and $R_1 = 1/\sigma_t$. When the contact junction is exposed to the high-power carriers, it acts as a weakly nonlinear source. Fig. 3(b) shows an equivalent circuit of the junction with a source current i_{PIM}

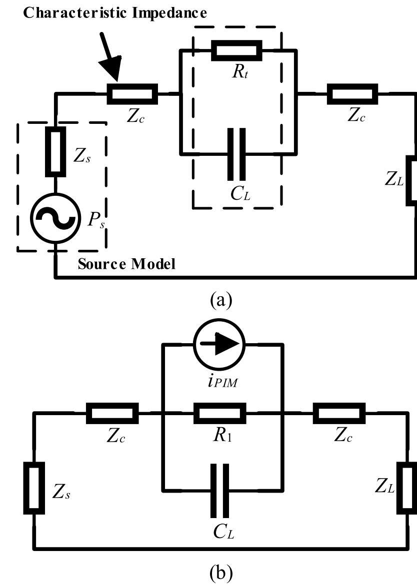

Fig. 3. Equivalent circuit of contact. (a) At carriers' frequencies. (b) At PIM frequencies.

which is a mixing product described by the tunneling current density multiplied by the real contact area when the total voltage at carriers' frequencies is represented by the sum of the carrier voltages given in (19).

It is necessary to note that our analysis is based on the approximation of a uniform current distribution at the contact spots. This allows us to model the contacts of rough surfaces with a random distribution of asperities of different sizes.

Nonlinearities of contact junctions are usually weak, and the mixing products that they generate are much weaker than the high-power carrier signals. Then the current of mixing products generated by the nonlinearity of R_t can be represented in the time domain by a few terms of the Taylor series

$$i(t) = \sum_{n=3}^{\infty} a_n v(t)^n. \quad (20)$$

When $i(t)$ and $v(t)$ are the current and voltage of nonlinear element R_t, respectively, $a_n = g_n A_r$ where the nonlinearity coefficients g_n are defined in (11) and (12) and the real contact area A_r is obtained from (17). The voltage $v(t)$ is the sum of the two carrier voltages of frequencies ω_1 and ω_2 with amplitudes defined in the steady-state regime in (19)

$$v(t) = |V_1|\cos(\omega_1 t + \theta_1) + |V_2|\cos(\omega_2 t + \theta_2) \quad (21)$$

where $|V_k|$ and θ_k are the voltage amplitude and phase at carrier frequencies ω_k, respectively. Substituting (21) in (20) and collecting the terms with the same frequencies allows us to obtain the mixing products. Then the currents of the third and fifth-order PIM products are

$$i_{\mathrm{PIM3}} = \frac{|V_1|^2|V_2|}{8}\left[6a_3 + 5a_5\left(2|V_1|^2 + 3|V_2|^2\right)\right] \times \cos((2\omega_1 - \omega_2)t + 2\theta_1 - \theta_2)$$
$$i_{\mathrm{PIM5}} = \frac{5a_5|V_1|^3|V_2|^2}{8}\cos((3\omega_1 - 2\omega_2)t + 3\theta_1 - 2\theta_2). \quad (22)$$

When the source impedance Z_s, the characteristic impedance of the transmission line Z_c, and the load impedance Z_L in the circuit of Fig. 3(b) are identical, the voltage

Authorized licensed use limited to: University of Liverpool. Downloaded on February 18,2024 at 11:08:21 UTC from IEEE Xplore. Restrictions apply.

This article has been accepted for inclusion in a future issue of this journal. Content is final as presented, with the exception of pagination.

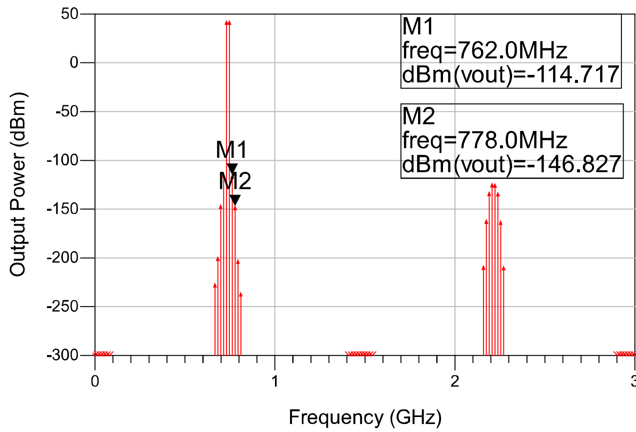

Fig. 4. ADS harmonic balance analysis of the equivalent circuit in Fig. 3. The PIM3 and PIM5 products, denoted M1 and M2, respectively, are in good agreement with the presented analysis.

magnitude at the load is approximately obtained at the PIM frequency as

$$\mathbf{V}_{\mathrm{PIM}} \simeq \frac{1}{2}\frac{R_1\mathbf{I}_{\mathrm{PIM}}}{\sqrt{1+(\omega_{\mathrm{PIM}}R_1C_L)^2}} \tag{23}$$

where the bold letters represent amplitudes of the cosine functions. The power of the output signal at the dBm scale is obtained at respective PIM frequencies as

$$P_{\mathrm{PIM}}[\mathrm{dBm}] = 10\log\left(\frac{\mathbf{V}_{\mathrm{PIM}}^2}{2Z_L}\right)+30. \tag{24}$$

The magnitudes of PIM3 and PIM5 products, calculated from (18) to (24), are −114.49 and −146.43 dBm, respectively, at frequencies $f_{\mathrm{PIM3}} = 2f_2 - f_1$ and $f_{\mathrm{PIM5}} = 3f_2 - 2f_1$, where $f_1 = 730$ MHz, $f_2 = 746$ MHz. They are obtained at $Z_L = Z_S = Z_c = 50\ \Omega$, $P_s = 20$ W, $C_L = 100$ nF, $a_1 = 100$ A/V, $a_3 = 10^5$ A/V^3, $a_5 = 10^9$ A/V^5, $R_1 = 1/a_1\ \Omega$. The results of the harmonic balance analysis of the equivalent circuit of Fig. 3(a) in ADS simulator are shown in Fig. 4 and demonstrate the high accuracy of the analytical model presented in this section.

V. Measurement Setup

The measurement setup for evaluating PIM products generated by MIM contact joints is shown in Fig. 5. In contrast to the test fixture used in [10], the contact junction is studied in a coaxial structure. An aluminum tube with a square cross section of 25.2 × 25.2 mm^2 and 3.3 mm thick walls acts as an outer conductor of the coaxial line. The total length of the tube split in two halves is 300 mm, and a continuous square-shaped inner conductor with a cross section of 7.95 × 7.95 mm^2 has the length of 234.8 mm measured between the centers of DIN 7/16 connectors. The connectors are attached at the distance of 37.5 mm from the open ends of the outer conductors, separated by a 2 mm wide slot in the middle, as shown in Fig. 5.

The hollow sections at the open ends of the enclosure have a cut-off frequency $f_c = 4.71$ GHz. Therefore, the two open ends of the fixture are well below the cut-off frequencies at the carrier frequencies $f_1 = 730$ MHz, $f_2 = 746$ MHz. So, the leakage of the TEM waves traveling in the coaxial line between the connectors is practically negligible. The PIM products of frequencies $f_{\mathrm{PIM3},L} = 714$ MHz,

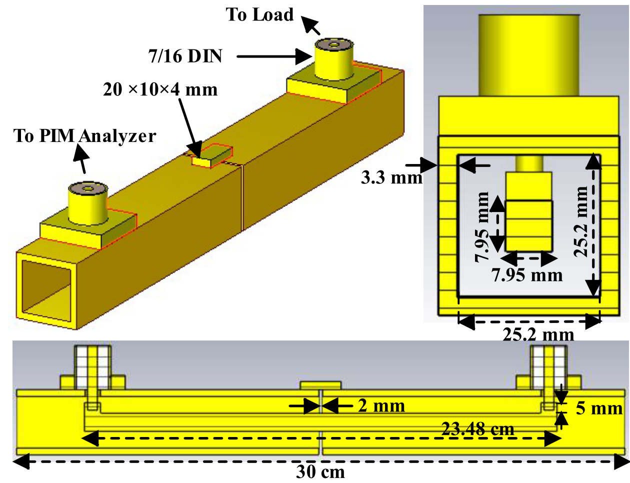

Fig. 5. Test device for PIM measurements in the 700 MHz band. An inner conductor is present only between the connectors. The hollow ends of the square aluminum enclosure have a cut-off frequency of 4.71 GHz.

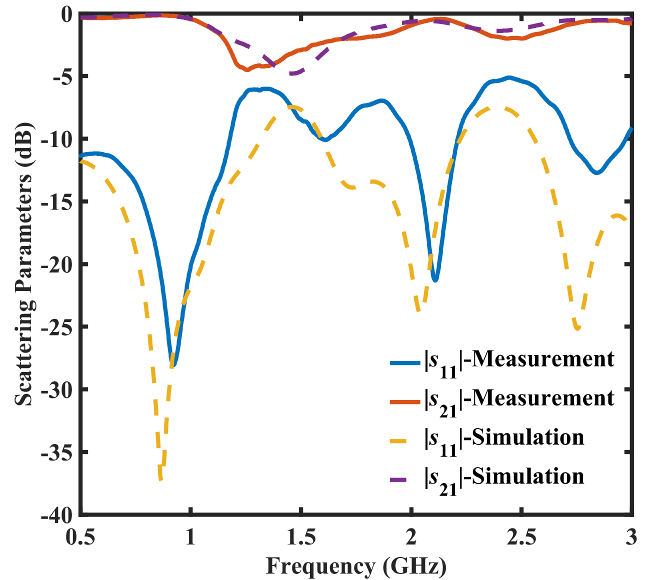

Fig. 6. Measured and simulated scattering parameter of the test device. At the reference frequency of 730 MHz, RL = 13.0 dB and IL = 0.27 dB.

$f_{\mathrm{PIM3},U} = 762$ MHz, and $f_{\mathrm{PIM5},L} = 698$ MHz, $f_{\mathrm{PIM5},U} = 778$ MHz are well below the f_c too.

The scattering characteristics of the test fixture with a 20 × 10 × 4 mm^3 conductor bridge between two halves of the outer conductor are illustrated in Fig. 6. They show that the return loss (RL) is 13.0 dB and the insertion loss (IL) is 0.27 dB at the carrier frequency of 730 MHz. When the conductor bridge connects the two halves of the waveguide enclosure, the carrier leakage through the slot is ∼1.1% at 730 MHz. However, such weak radiation strongly affects the measured PIM when the contact of the bridge with the waveguide is loose. The CST simulations, validated against the measurements, confirm that the bridge current obtained from (18) is 2.26% lower than the corresponding value obtained from CST at 730 MHz.

A. DC Resistance of Contact Junctions

The gap between the two halves of the waveguide enclosure shown in Fig. 5 is bridged by an aluminum (Al) strip in

Authorized licensed use limited to: University of Liverpool. Downloaded on February 18,2024 at 11:08:21 UTC from IEEE Xplore. Restrictions apply.

This article has been accepted for inclusion in a future issue of this journal. Content is final as presented, with the exception of pagination.

Fig. 7. Four-wire test setup for measuring dc resistance versus pressure. The bridge is the only contact between the two halves of the aluminum tube with the $m\Omega$ resistance. The dc contact resistance is measured with a Keithley DMM6500 digital multimeter at variable pressure on the contact plate.

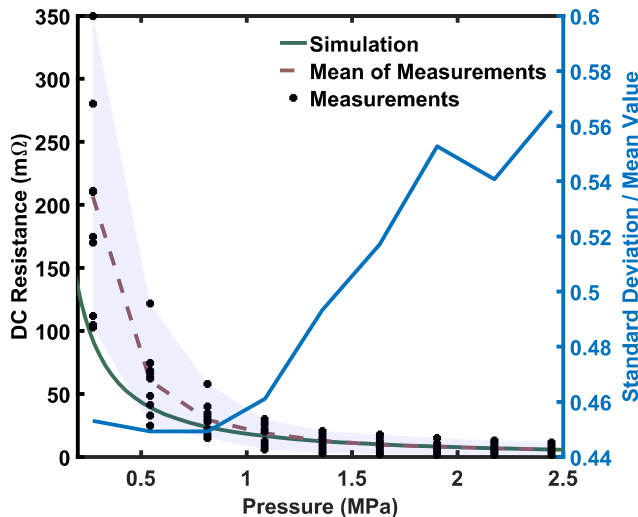

Fig. 8. Measured and simulated dependence of the dc resistance on the contact pressure along with the normalized standard deviation. The simulation parameters: the contact size is 2×1 cm^2, $L = 1.41$ cm, $\gamma = 1.5$, $D = 2.4$, $G = 5 \times 10 - 11$, $E = 70$ GPa, Poisson ratio of metals $\upsilon = 0.33$, the yield strength $Y = 270$ MPa, $K = H/Y = 2.8$ where H is the hardness, $s = 0.925$ nm, $\phi_0 = 2.95$ eV, and oxide permittivity $\varepsilon_r = 9.3$.

the middle. When the pressure is applied to the bridge, variations of the contact resistance are measured with a four-wire test setup (Kelvin clips). The force applied to the Al strip is measured by the gauge (TopHomer 500 N) shown in Fig. 7. The test results are averaged over ten measurements at each pressure varying from 0.2 to 2.5 MPa. Surface roughness of a few microns is simulated at the parameters $\gamma = 1.5$, $D = 2.4$, and $G = 5 \times 10^{-11}$ used earlier for the realistic surface profiles in [34]. The chosen potential barrier height for Al_2O_3 is half of its bandgap [31]. The simulated and the measured mean values of the dc resistance are shown in Fig. 8 and demonstrate a good correlation at pressure values exceeding 1.3 MPa.

B. RF Resistance of Contact Junctions

In contrast to dc current in the bridging strip, which occupies the whole of its volume at the contact junction, RF current is confined to the proximity of the slot in the waveguide enclosure. As a result, the RF current is crowded near the slot edges. Therefore, it is necessary to assess the relationship

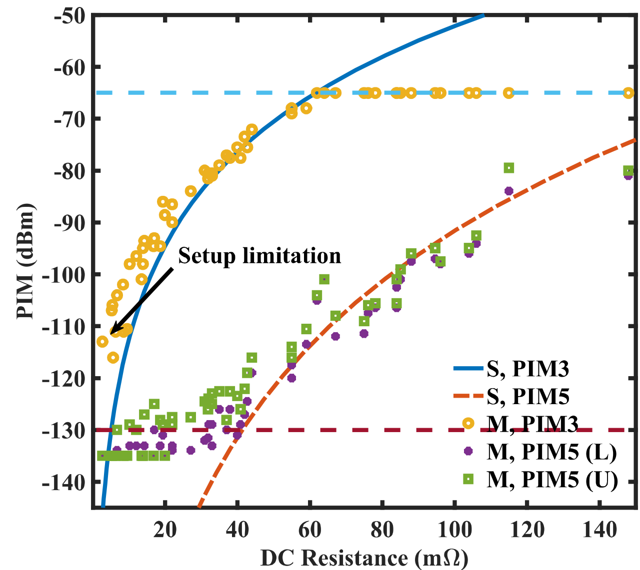

Fig. 9. Simulated (S) and measured (M) PIM3 and PIM5 products at carrier power 2×43 dBm in the 700 MHz band. The input parameters are retrieved from the measured resistances and the RF Ratio $\delta = 0.05$. $f_1 = 730$ MHz, $f_2 = 746$ MHz, $f_{\mathrm{PIM3}} = 714$ MHz, f_{PIM5}, $L = 698$ MHz, f_{PIM5}, and $U = 778$ MHz.

between the dc and RF current patterns in the contact bridge. Their ratio is represented by parameter δ which is obtained by fitting the PIM3 curves in the 700 MHz band.

The PIM3 and PIM5 products versus dc resistance of the contact joint are obtained from the model described in Sections II–IV. They are compared in Fig. 9 with the measurement results obtained by CCI PIMPro 700 PIM analyzer at an input power of 2×43 dBm. These plots provide insight into the accuracy of the models used for PIM product predictions.

At low pressure, the contact resistance is high and represents a dominant PIM source. Then the model, based on $\delta = 0.05$ for the ratio of RF contact area to dc contact area, predicts PIM3 fairly well. When the contact pressure increases, the junction resistance reduces, and its nonlinearity becomes comparable with other nonlinearities of the measurement setup. Then the test results deviate from the simulations. It has been also observed that the level of PIM5 products in the upper band of 778 MHz is always higher than in the lower band of 698 MHz.

The measured and simulated PIM3 products are shown in Fig. 10 in dependence on the contact pressure. The tests are performed at the carrier input powers of 2×43 and 2×30 dBm at each pressure. They allow us to assess the slope of PIM3 products versus input power. All measurement results exhibit a slope of 3 dB per dB at the contact pressures less than 1.4 MPa but above 1.4 MPa the slope decreases. At high contact pressure, the PIM3 level decreases and becomes comparable to the residual PIM level of the test setup. The variation in measurements is possibly caused by the non-uniformity of the actual surface profile. The mechanical model discussed in this article presents the average contact area for different realizations of the WM function. Nonetheless, given the large size of the contact area, it can be represented statistically, leading to an expected value that closely aligns with this average. However, it is important to consider that real-world surfaces deviate from uniform profiles

Authorized licensed use limited to: University of Liverpool. Downloaded on February 18,2024 at 11:08:21 UTC from IEEE Xplore. Restrictions apply.

This article has been accepted for inclusion in a future issue of this journal. Content is final as presented, with the exception of pagination.

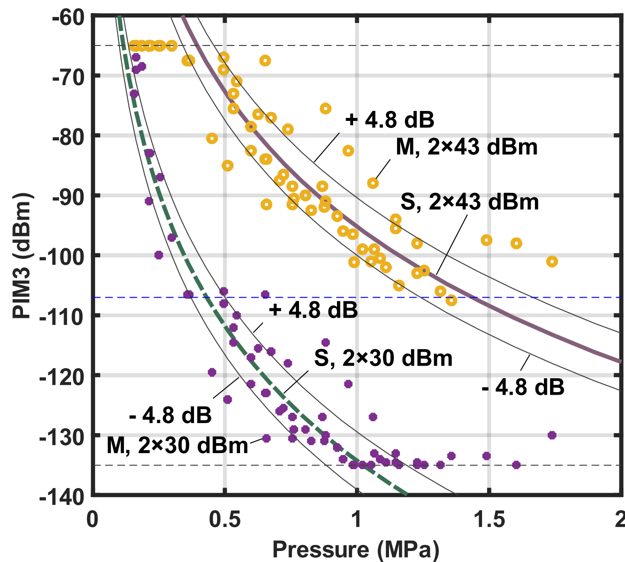

Fig. 10. Simulated (S) and measured (M) PIM3 as a function of pressure in the 700 MHz band (f_1 = 730 MHz, f_2 = 746 MHz, f_{PIM3} = 714 MHz). The measurement data are well aligned with the simulations within ±4.8 dB deviation limits. The blue dashed line represents the residual PIM3 of the test setup at 43 dBm carrier power.

and may also exhibit waviness, which was not accounted in the current model. It is noteworthy that the presented model assumes a constant oxide thickness, neglecting its potential variations that can contribute to the measurement variations.

VI. Conclusion

A detailed study of PIM in contact joints of conductors with rough surfaces has been presented. An advanced nonlinear model of contact junction is proposed based on the analysis of the charge tunneling in MIM contacts with a fractal profile of contact surfaces. The presented model enables an accurate analysis of PIM generation in the MIM structures with a sub-nanometer insulating layers. The model has been validated experimentally and by a comparison with the WKB numerical analysis and the Simmons model. The simulated conductor joints are measured using a test fixture based on the slotted coaxial waveguide. The effect of contact pressure on both the contact resistance and PIM products is evaluated in the frequency band of 700 MHz. The model parameters deduced from the PIM3 measurements enable prediction of the PIM5 products without the need of adjusting the model parameters. The presented model provides insight into the mechanisms of PIM generation at the contact junctions and facilitates the design of the low-PIM RF front ends of the communication systems.

References

[1] M. Bayrak and F. A. Benson, "Intermodulation products from nonlinearities in transmission lines and connectors at microwave frequencies," *Proc. Inst. Elect. Eng.*, vol. 122, pp. 361–367, Apr. 1975.

[2] W. H. Higa, "Spurious signals generated by electron tunneling on large reflector antennas," *Proc. IEEE*, vol. 63, no. 2, pp. 306–313, Feb. 1975.

[3] C. D. Bond, C. S. Guenzer, and C. A. Carosella, "Intermodulation generation by electron tunneling through aluminum-oxide films," *Proc. IEEE*, vol. 67, no. 12, pp. 1643–1652, Dec. 1979.

[4] A. P. Foord and A. D. Rawlings, *A Study of Passive Intermodulation Interference in Spce RF Hardware*. Kent, U.K.: Univ. Kent, May 1992.

[5] P. Bolli, S. Selleri, and G. Pelosi, "Passive intermodulation on large reflector antennas," *IEEE Antennas Propag. Mag.*, vol. 44, no. 5, pp. 13–20, Oct. 2002.

[6] C. Vicente and H. L. Hartnagel, "Passive-intermodulation analysis between rough rectangular waveguide flanges," *IEEE Trans. Microw. Theory Techn.*, vol. 53, no. 8, pp. 2515–2525, Aug. 2005.

[7] J. Russer, A. Ramachandran, A. Cangellaris, and P. Russer, "Phenomenological modeling of passive intermodulation (PIM) due to electron tunneling at metallic contacts," in *IEEE MTT-S Int. Microw. Symp. Dig.*, Jun. 2006, pp. 1129–1132.

[8] S. Zhang, X. Zhao, F. Gao, and Y. He, "Study of metal contact resistance and its statistical correlationship with passive intermodulation," in *Proc. IEEE Holm Conf. Electr. Contacts*, Oct. 2018, pp. 353–358.

[9] Q. Jin, J. Gao, G. T. Flowers, Y. Wu, and H. Huang, "Passive intermodulation models of current distortion in electrical contact points," *IEEE Microw. Wireless Compon. Lett.*, vol. 29, no. 3, pp. 180–182, Mar. 2019.

[10] S. Zhang, X. Zhao, Z. Cao, K. Zhang, F. Gao, and Y. He, "Experimental study of electrical contact nonlinearity and its passive intermodulation effect," *IEEE Trans. Compon., Packag., Manuf. Technol.*, vol. 10, no. 3, pp. 424–434, Mar. 2020.

[11] A. Dayan, Y. Huang, and A. Schuchinsky, "Passive intermodulation at contacts of rough conductors," *Electron. Mater.*, vol. 3, no. 1, pp. 65–81, Feb. 2022.

[12] R. Holm, "The electric tunnel effect across thin insulator films in contacts," *J. Appl. Phys.*, vol. 22, no. 5, pp. 569–574, May 1951.

[13] J. G. Simmons, "Generalized formula for the electric tunnel effect between similar electrodes separated by a thin insulating film," *J. Appl. Phys.*, vol. 34, no. 6, pp. 1793–1803, Jan. 1963.

[14] J. C. Fisher and I. Giaever, "Tunneling through thin insulating layers," *J. Appl. Phys.*, vol. 32, no. 2, pp. 172–177, Feb. 1961.

[15] P. Zhang, "Scaling for quantum tunneling current in nano- and subnano-scale plasmonic junctions," *Sci. Rep.*, vol. 5, no. 1, p. 9826, May 2015.

[16] A. Dayan, Y. Huang, and A. Schuchinsky, "Contact nonlinearities of rough conductors in antennas and connectors," in *Proc. 17th Eur. Conf. Antennas Propag. (EuCAP)*, Mar. 2023, pp. 1–4.

[17] J. R. Wilkerson, K. G. Gard, A. G. Schuchinsky, and M. B. Steer, "Electro-thermal theory of intermodulation distortion in lossy microwave components," *IEEE Trans. Microw. Theory Techn.*, vol. 56, no. 12, pp. 2717–2725, Dec. 2008.

[18] R. H. Fowler and L. Nordheim, "Electron emission in intense electric fields," *Proc. Roy. Soc. London, A, Containing Papers Math. Phys. Character*, vol. 119, no. 781, pp. 173–181, May 1928.

[19] E. L. Murphy and R. H. Good, "Thermionic emission, field emission, and the transition region," *Phys. Rev.*, vol. 102, no. 6, pp. 1464–1473, Jun. 1956.

[20] L. Kogut and K. Komvopoulos, "Electrical contact resistance theory for conductive rough surfaces," *J. Appl. Phys.*, vol. 94, no. 5, pp. 3153–3162, Sep. 2003.

[21] B. Nikolić and P. B. Allen, "Electron transport through a circular constriction," *Phys. Rev. B, Condens. Matter*, vol. 60, no. 6, pp. 3963–3969, Aug. 1999.

[22] D. Bohm, *Quantum Theory, Mineola*. New York, NY, USA: Dover, 1989.

[23] J. A. Greenwood, "Constriction resistance and the real area of contact," *Brit. J. Appl. Phys.*, vol. 17, no. 12, pp. 1621–1632, Dec. 1966.

[24] P. R. Nayak, "Random process model of rough surfaces," *Amer. Soc. Mech. Eng. (ASME), J. Lubrication Tech.*, vol. 93, pp. 398–407, Jul. 1971.

[25] R. S. Sayles and T. R. Thomas, "Surface topography as a nonstationary random process," *Nature*, vol. 271, no. 5644, pp. 431–434, Feb. 1978.

[26] M. V. Berry, Z. Lewis, and J. F. Nye, "On the Weierstrass–Mandelbrot fractal function," *Proc. Roy. Soc.*, vol. 370, pp. 459–484, Apr. 1980.

[27] B. B. Mandelbrot, *The Fractal Geometry of Nature*. San Francisco, CA, USA: W. H. Freeman, 1982.

[28] M. Ausloos and D. H. Berman, "A multivariate Weierstrass-Mandelbrot function," *Proc. Roy. Soc. London A, Math. Phys. Sci.*, vol. 400, no. 1819, pp. 331–350, 1819.

[29] W. Yan and K. Komvopoulos, "Contact analysis of elastic-plastic fractal surfaces," *J. Appl. Phys.*, vol. 84, no. 7, pp. 3617–3624, Oct. 1998.

[30] L. Kogut and K. Komvopoulos, "Electrical contact resistance theory for conductive rough surfaces separated by a thin insulating film," *J. Appl. Phys.*, vol. 95, no. 2, pp. 576–585, Jan. 2004.

[31] L. Kogut and K. Komvopoulos, "Analytical current–voltage relationships for electron tunneling across rough interfaces," *J. Appl. Phys.*, vol. 97, no. 7, pp. 073701-1–073701-5, Apr. 2005.

[32] R. L. Jackson and J. L. Streator, "A multi-scale model for contact between rough surfaces," *Wear*, vol. 261, nos. 11–12, pp. 1337–1347, Dec. 2006.

Authorized licensed use limited to: University of Liverpool. Downloaded on February 18,2024 at 11:08:21 UTC from IEEE Xplore. Restrictions apply.

This article has been accepted for inclusion in a future issue of this journal. Content is final as presented, with the exception of pagination.

[33] O. Rezvanian, M. A. Zikry, C. Brown, and J. Krim, "Surface roughness, asperity contact and gold RF MEMS switch behavior," *J. Micromech. Microeng.*, vol. 17, no. 10, pp. 2006–2015, Oct. 2007.

[34] O. Rezvanian et al., "The role of creep in the time-dependent resistance of ohmic gold contacts in radio frequency microelectromechanical system devices," *J. Appl. Phys.*, vol. 104, no. 2, pp. 024513-1–024513-3, Jul. 2008.

[35] W. E. Wilson, S. V. Angadi, and R. L. Jackson, "Surface separation and contact resistance considering sinusoidal elastic–plastic multi-scale rough surface contact," *Wear*, vol. 268, nos. 1–2, pp. 190–201, Jan. 2010.

[36] R. L. Jackson, E. R. Crandall, and M. J. Bozack, "Rough surface electrical contact resistance considering scale dependent properties and quantum effects," *J. Appl. Phys.*, vol. 117, no. 19, May 2015, Art. no. 195101.

[37] K. Komvopoulos, "A multiscale theoretical analysis of the mechanical, thermal, and electrical characteristics of rough contact interfaces demonstrating fractal behavior," *Frontiers Mech. Eng.*, vol. 6, pp. 1–20, Jul. 2020.

[38] C. Vicente, D. Wolk, H. L. Hartnagel, B. Gimeno, V. E. Boria, and D. Raboso, "Experimental analysis of passive intermodulation at waveguide flange bolted connections," *IEEE Trans. Microw. Theory Techn.*, vol. 55, no. 5, pp. 1018–1028, May 2007.

[39] X. Zhao et al., "Analytic passive intermodulation model for flange connection based on metallic contact nonlinearity approximation," *IEEE Trans. Microw. Theory Techn.*, vol. 65, no. 7, pp. 2279–2287, Jul. 2017.

[40] K. Zhang, T. Li, and J. Jiang, "Passive intermodulation of contact nonlinearity on microwave connectors," *IEEE Trans. Electromagn. Compat.*, vol. 60, no. 2, pp. 513–519, Apr. 2018.

Amir Dayan received the B.Sc. degree in electronic engineering from the University of Kashan, Kashan, Iran, in August 2015, and the M.Sc. degree in communication fields and waves from the Amir Kabir University of Technology, Tehran, Iran, in February 2018. He is currently pursuing the Ph.D. degree at the Department of Electrical Engineering and Electronics, University of Liverpool, Liverpool, U.K.

His research interests include electromagnetic interference, passive intermodulation in metal contacts, common-mode noise mitigation in high-frequency printed circuit boards, and numerical analysis of Maxwell's equations.

Yi Huang (Fellow, IEEE) received the B.Sc. degree in physics from Wuhan University, Wuhan, China, in 1984, the M.Sc.(Eng.) degree in microwave engineering from the Nanjing Research Institute of Electronics Technology (NRIET), Nanjing, China, in 1987, and the D.Phil. degree in communications from the University of Oxford, Oxford, U.K., in 1994.

His experience includes three years spent with NRIET, as a Radar Engineer and various periods with the Universities of Birmingham, Oxford, and Essex, U.K., as a Member of Research Staff. In 1994, he worked as a Research Fellow with the British Telecom Laboratories, Ipswich, U.K., and then, he joined the Department of Electrical Engineering and Electronics, University of Liverpool, Liverpool, U.K., as a Faculty, in 1995, where he is currently a Full Professor of wireless engineering, the Head of the High-Frequency Engineering Group, and the Deputy Head of the Department. He has published over 500 refereed articles in leading international journals and conference proceedings and authored four books, including *Antennas: From Theory to Practice* (John Wiley, 2008 and 2021). He has received many patents, and research grants from research councils, government agencies, charities, E.U., and industry. His research interests include antennas, wireless communications, applied electromagnetics, radar, and EMC. More recently, he is focused on mobile antennas, wireless energy harvesting, and power transfer.

Prof. Huang is a Fellow of IET. He was a recipient of over ten awards. He has served on several national and international technical committees and has been an Editor, an Associate Editor, or a Guest Editor of five international journals. In addition, he has been a keynote/invited speaker and organizer of many conferences and workshops. He is the Editor-in-Chief of Wireless Engineering and Technology, an Associate Editor of IEEE TRANSACTION ON ANTENNAS AND PROPAGATION, and the U.K./Ireland Representative of the European Association of Antenna and Propagation (EurAAP), from 2016 to 2020.

Mattias Gustafsson received the M.Sc.E.E. degree from the Chalmers University of Technology, Göteborg, Sweden, in 1997.

His past industry career was dominated by the design and systemization of RF systems, microwave components, and antennas. In recent years, he has been involved in more general perspectives concerning the research of radio communication systems. Currently, he is the Team Leader of the Base Transceiver Systems Research with Huawei Technologies Sweden, Gothenburg, Sweden.

Torbjörn Olsson (Member, IEEE) received the Ph.D. degree in experimental atomic physics from the Chalmers University of Technology, Göteborg, Sweden, in 1987.

After post-doctoral positions with the Jesse W. Beams Laboratory, Charlottesville, VA, USA, and the Royal Institute of Technology, Stockholm, Sweden. In 1993, he is with the mobile phone industry and works currently through his own company Scipovi AB as a Consultant for Huawei Sweden AB, Gothenburg, Sweden. He, together with coauthors, received the IEEE 2001 Microwave Prize for a contribution to the study of microwave breakdown in resonators and filters.

Alexander G. Schuchinsky (Fellow, IEEE) received the Ph.D. degree in radiophysics from Leningrad Electrotechnical University (USSR), Saint Petersburg, Russia, in 1983.

He holds the academic title of Senior Research Scientist. From 1973 to 1994, he was with the Microwave Electromagnetics Laboratory, Rostov State University, Rostov-on-Don, Russia. From 1994 to 2002, he was a Chief Engineer with Deltec-Telesystems, Wellington, New Zealand. From 2002 to 2015, he was a Reader with Queen's University Belfast, Belfast, U.K. He is Currently an Honorary Fellow with the University of Liverpool, Liverpool, U.K. He has authored three international patents, five book chapters and over 250 refereed journal and conference papers. His research interests include the mechanisms of PIM, hexaferrites and self-biased nonreciprocal devices, and passive nonlinearities in microwave circuits.

Dr. Schuchinsky was a founding member of the European Virtual Institute for Artificial Electromagnetic Materials and Metamaterials where he served on the Board of Directors. He was a co-founder and member of the Steering Committee of the European Doctoral Programs on Metamaterials. He was a Member of the European Physical Society and a Fellow of the Higher Education Academy, U.K. He was a co-recipient of the IEEE 2010 Microwave Prize and the 2012 V.G. Sologub Award for contribution to Computational Electromagnetics. He was the Co-Founder and the General Co-Chair of the series of annual conferences "Metamaterials-International Congress on Advanced Electromagnetic Materials in Microwaves and Optics."

Authorized licensed use limited to: University of Liverpool. Downloaded on February 18,2024 at 11:08:21 UTC from IEEE Xplore. Restrictions apply.